Nanoscale

PAPER

View Article Online
View Journal | View Issue

Check for updates

Cite this: *Nanoscale*, 2026, **18**, 3377

3D Au nanoparticle lattices in MoO_3 for tunable optical and thermo-electrical properties

Senad Isaković, [a,b] Juraj Držić,[c] Ivana Periša,[c] Tihomir Car, [c] Sigrid Bernstorff, [d] Maja Đekić[b] and Maja Mičetić *[c]

Received 15th September 2025,
Accepted 13th December 2025

DOI: 10.1039/d5nr03899e

rsc.li/nanoscale

Incorporating noble-metal nanoparticles into semiconductors offers a powerful means to tailor their functional properties. Here, we demonstrate that embedding ordered three-dimensional lattices of Au nanoparticles (Au NPs) into MoO_3 thin films *via* magnetron sputtering enables broad tunability of the optical and thermo-electrical behavior. The formation of regular Au NP lattices, with controlled particle sizes, interparticle separations, and ordering, is achieved through precise adjustment of the deposition temperature and layer thickness conditions. Localized surface plasmon resonances (LSPR) arising from Au NPs-and their coupling at small separations-induce a strong modulation of the optical absorption across a wide spectral range. Simultaneously, the film's electrical resistance can be tuned by up to six orders of magnitude, while the activation energy and temperature coefficient of resistance (TCR) are reduced by up to fifty-fold compared to pure MoO_3. These findings offer relevant information for designing oxide–plasmonic hybrid materials, highlighting their potential for next-generation optoelectronic, sensing, and energy-harvesting devices.

Open Access Article. Published on 13 January 2026. Downloaded on 5/1/2026 4:58:18 PM.
This article is licensed under a Creative Commons Attribution 3.0 Unported Licence.

1. Introduction

Molybdenum trioxide (MoO_3) is a wide-bandgap transition metal oxide semiconductor (>3 eV) that combines high electrochemical activity, chemical stability, and photochromic, thermochromic, and catalytic functionalities.[1–7] These attributes underpin its widespread use in applications ranging from photovoltaics and lithium-ion batteries to gas sensors, electrochromic devices, and other optoelectronic technologies.[8–11] Achieving optimal performance in such applications requires precise control of the MoO_3's optoelectronic properties. In particular, its intrinsically poor electrical conductivity and the relatively large activation energy associated with its temperature coefficient of resistance (TCR) often limit the device performance, motivating strategies such as doping and nanostructuring to tailor these properties.[12–15]

Metal atom or nanoparticle (NP) doping has proven especially effective in enhancing the sensing, photoelectric, electrochemical, and catalytic behavior of MoO_3.[16–20] Noble-metal NPs are of particular interest because their localized surface plasmon resonances (LSPR) enable a powerful modulation of the optical and electrical properties, with tunability governed by the NP size, shape, and spacing.[21–26] Gold (Au) NPs stand out in this regard: plasmonic coupling between closely spaced Au NPs can strongly reshape absorption spectra, while simultaneously influencing charge transport in poorly conducting semiconductors.[27–32] To date, most studies have focused on Au nanostructures deposited onto the surface of MoO_3 thin films, whereas the formation of ordered Au NP assemblies within MoO_3 remains largely unexplored. Embedding three-dimensional (3D) Au NP lattices directly inside the MoO_3 matrix provides new opportunities to simultaneously manipulate light absorption and electrical transport, while retaining the structural and chemical stability of the oxide host. Embedding ordered plasmonic lattices in wide-bandgap oxides thus provides a unique route to engineer multifunctional materials that simultaneously combine optical tunability, electrical transport modulation, and thermal stability-properties crucial for nanoscale optoelectronic applications.

A study of Au + MoO_3 mixture, resulting in spatially arranged Au NPs in MoO_3 was reported by our group several years ago.[32] In that work, Au NPs were uniformly distributed throughout the film thickness due to continuous co-deposition of Au and MoO_3. The films exhibited LSPR features and electrical properties dependent on Au concentration. Although these tunable properties are of great interest for tailoring MoO_3 functionalities, a clear relationship between Au NP size,

[a]*University of Zagreb, Faculty of Physics, Bijenička cesta 32, 10000 Zagreb, Croatia*
[b]*Faculty of Science, University of Sarajevo, Zmaja od Bosne 33, 71 000 Sarajevo, Bosnia and Herze-govina*
[c]*Ruđer Bošković Institute, Bijenička cesta 54, 10000 Zagreb, Croatia. E-mail: maja.micetic@irb.hr*
[d]*Elettra-Sincrotrone Trieste S.C.p.A., Strada Statale 14 km 163.5 in AREA Science Park, 34149 Basoviz-za/Trieste, Italy*

Open Access Article. Published on 13 January 2026. Downloaded on 5/1/2026 4:58:18 PM.
This article is licensed under a Creative Commons Attribution 3.0 Unported Licence.

separation, and the resulting opto-electrical and thermal properties could not be established.

The present study uses a multilayer approach which enables controlled formation of well-defined, three-dimensional Au NP lattices with tunable interparticle spacing and ordering. This allows us, for the first time, to systematically correlate structural parameters with optical and thermo-electrical behavior. We demonstrate the fabrication of MoO_3 thin films containing 3D ordered Au NP lattices using magnetron sputtering of alternating (Au + MoO_3)/MoO_3 multilayers. We show that lattice formation occurs under specific Au + MoO_3 layer thickness and temperature conditions (RT to 500 °C), resulting in tunable NP dimensions, spacing, and ordering. These structural features lead to profound changes in functionality: (i) the optical absorption is strongly modified through LSPR coupling, (ii) the electrical resistance can be tuned across several orders of magnitude, and (iii) the activation energy and TCR are greatly reduced. This work thus establishes a scalable route for embedding ordered plasmonic lattices into semiconducting oxides, providing a versatile platform for next-generation opto-electronic, sensing, and thermo-electrical devices.

2. Materials and methods

Thin films of Au–MoO_3 nanocomposites are deposited using a CMS-18 multisource magnetron sputtering system (K. J. Lesker) using (Au + MoO_3)/MoO_3 multilayer growth driven self-assembly.[33,34] A 3-inch Au target (99.99%) is sputtered in DC mode and a MoO_3 target (99.99%) in RF mode onto Si (100) and glass substrates. The base chamber pressure prior to deposition is 8×10^{-6} Pa. Three series of films containing ordered Au NP lattices are prepared by varying sputtering power, deposition time, and substrate temperature:

- Series 1 (Au1T1–Au3T1): Deposited at 30 °C with constant sputtering powers (Au: 6 W, MoO_3: 100 W), while varying the deposition time of the Au + MoO_3 layer.
- Series 2 (Au4T1–Au4T3): Deposited with sputtering powers of 15 W (Au) and 100 W (MoO_3), and fixed deposition times (45 s for the Au + MoO_3 layer, 80 s for MoO_3), while varying the substrate temperature.
- Series 3 (Au1T2–Au1T4): Deposited with the same sputtering powers as Series 1, while varying the substrate temperature from 200 °C to 500 °C.

The sample nomenclature reflects the Au content (Au1–Au4, defined by the Au sputtering power and deposition time) and the deposition temperature (T1–T4).

A similar fabrication approach has been successfully applied to thin films with embedded semiconductor and metallic nanoparticles.[24,31,34–38] The deposition parameters are summarized in Table 1.

The film structure, including the NP size, shape, and ordering, is investigated by grazing-incidence small-angle X-ray scattering (GISAXS) at the Austrian SAXS beamline of Elettra-Sincrotrone (Trieste, Italy) using 8 keV photons and a Pilatus3 1M detector (Dectris Ltd, Switzerland).

Table 1 Deposition parameters of Au–MoO_3 films. P_{Au} and P_{MoO_3} are the sputtering powers of Au and MoO_3, respectively; t_d is the deposition time of each (Au + MoO_3)/MoO_3 bilayer; T_d is the deposition temperature. The last two columns show the Au and Mo areal densities as determined by RBS

Sample/par	Composition	(P_{Au} + P_{MoO_3})/P_{MoO_3} (W)	t_d (s)	T_d (°C)	Au (10^{15} at cm^{-2})	Mo (10^{15} at cm^{-2})
Au1T1	(Au + MoO_3)/MoO_3 × 20	(6 + 100)/100	45/80	30	83	126
Au2T1	(Au + MoO_3)/MoO_3 × 20	(6 + 100)/100	60/80	30	93	168
Au3T1	(Au + MoO_3)/MoO_3 × 20	(6 + 100)/100	80/80	30	224	106
Au4T1	(Au + MoO_3)/MoO_3 × 20	(15 + 100)/100	45/80	30	190	190
Au4T2	(Au + MoO_3)/MoO_3 × 20	(15 + 100)/100	45/80	200	190	190
Au4T3	(Au + MoO_3)/MoO_3 × 20	(15 + 100)/100	45/80	300	190	190
Au1T2	(Au + MoO_3)/MoO_3 × 20	(6 + 100)/100	45/80	200	86	113
Au1T3	(Au + MoO_3)/MoO_3 × 20	(6 + 100)/100	45/80	300	86	113
Au1T4	(Au + MoO_3)/MoO_3 × 20	(6 + 100)/100	45/80	500	86	113

Scanning electron microscopy (SEM) measurements are performed using the thermal field emission scanning electron microscope (FE SEM, model JSM-7000 F, by JEOL Ltd, Tokyo, Japan), linked to the energy-dispersive X-ray analyzer EDS/INCA 350, Oxford Instruments Ltd (Abingdon, UK).

Crystalline phases are characterized by grazing-incidence X-ray diffraction (XRD) with a Bruker D8 Advance diffractometer (Cu Kα, λ = 0.154 nm, 40 kV, 40 mA) using a LynxEye detector.

The elemental composition is determined by Rutherford backscattering spectrometry (RBS) using a 6 MV tandem Van de Graaff accelerator (Ruđer Bošković Institute) with a 2.4 MeV Si ion beam.

The electrical resistance is measured using a Keithley 6517B sourcemeter for high-resistance films with data acquisition *via* LabView. Measurements are carried out between 10 °C and 90 °C, with the applied voltage adjusted to the film resistivity. Four thin Cu wires are attached to the film corners with temperature-resistant Ag paste. The size of the rectangular samples for the electrical measurements are 1 × 1 cm^2.

Optical transmission and reflectance spectra are recorded using an Ocean Optics system consisting of a deuterium–halogen light source (DH-2000-BAL, 210–2500 nm), a UV/VIS spectrometer (HR4000), and SpectraSuite software.

3. Results and discussion

3.1. Structural properties of the films

3.1.1. Nanoparticle formation and their size-arrangement properties. The spatial organization of the Au nanoparticles

This journal is © The Royal Society of Chemistry 2026

Open Access Article. Published on 13 January 2026. Downloaded on 5/1/2026 4:58:18 PM.
This article is licensed under a Creative Commons Attribution 3.0 Unported Licence.

(NPs) within the MoO_3 matrix is analyzed using grazing-incidence small-angle X-ray scattering, a powerful technique capable of probing long-range ordering and size properties across billions of nanostructures simultaneously.[39–43] Representative GISAXS maps, numerical simulations, and schematic lattice models are shown in Fig. 1. Distinct horizontal sheets (green arrows) appear in most samples, arising from the multilayered deposition sequence. The number of sheets is inversely related to the multilayer thickness: for example, Au3T1 (Fig. 1c) exhibits four sheets, while Au1T1 shows only two. Lateral scattering peaks (yellow arrows) reveal in-plane ordering of NPs, with their positions along the Q_y axis directly related to the NP spacing. Similar, comparative microscopyGISAXS analyses of 3D-ordered NP systems can be found in ref. 39 and 40. In Au3T1, the ring-like shape of these peaks indicates vertical correlation of the NP positions within each layer, consistent with the presence of multiple NP sublayers per MoO_3 spacer. Previous studies report vertical separations of about 2 nm, much smaller than the overall multilayer period, in good agreement with our earlier observations.[34] In contrast, Au4T1–Au4T3 films (higher Au content) display sharp higher-order peaks (pink arrows), characteristic of well-ordered three-dimensional (3D) body-centered tetragonal (BCT) lattices with correlated ordering in both lateral and vertical directions.

Thus, samples with low Au content (Au1–Au3 series) form multilayered arrangements containing one to three NP sublayers per MoO_3 layer, while those with higher Au incorporation (Au4 series) evolve into highly ordered 3D BCT lattices. Increasing the temperature of deposition leads to an increased size and spacing of NP, yet the BCT ordering is preserved up to 300 °C. At 500 °C (Au1T4), however, GISAXS shows only diffuse scattering, indicating the loss of long-range order and thus a random NP distribution.

A quantitative analysis of the GISAXS patterns is performed using the model of Buljan *et al.*,[39] which accounts for deviations from the ideal lattice positions and NP size distributions. The NP lattices are modeled as BCT arrays with short-range order, defined by lateral ($\vec{a_1}$, $\vec{a_2}$) and vertical ($\vec{a_3}$) basis vectors. Deviations from the ideal positions are parameterized ($\sigma_{1,2}^{x,y}$, $\sigma_3^{x,y}$, $\sigma_{1,2}^{z}$, σ_3^{z}), while NP shape is approximated as spheroidal with lateral radius R_L, vertical radius R_V, and size distribution σ_R. The shape of such small gold NPs produced by sputtering techniques is usually spherical or spheroidal.[44,45] The GISAXS intensity distributions indicate an averaged shape function that is fully spheroidal to spherical, implying that if small facets exist, they are randomly oriented. SEM measurements (Fig. S1, SI) reveal that only the largest Au NPs (Au4T3) are resolvable, appearing spherical without visible faceting.

Simulated maps (insets, Fig. 1) reproduce experimental patterns with high fidelity, validating the extracted structural parameters (Table 2). The dependence of lattice constants (a,c ($a = a_1^x = a_1^y = a_2^x = a_2^y$,$c = a_3^z$)) and NP diameters ($D_L$,$D_V$) on the deposition parameters is summarized in Fig. 2. Increasing Au deposition time reduces both the lateral and vertical spacings, while the deposition temperature primarily affects the vertical

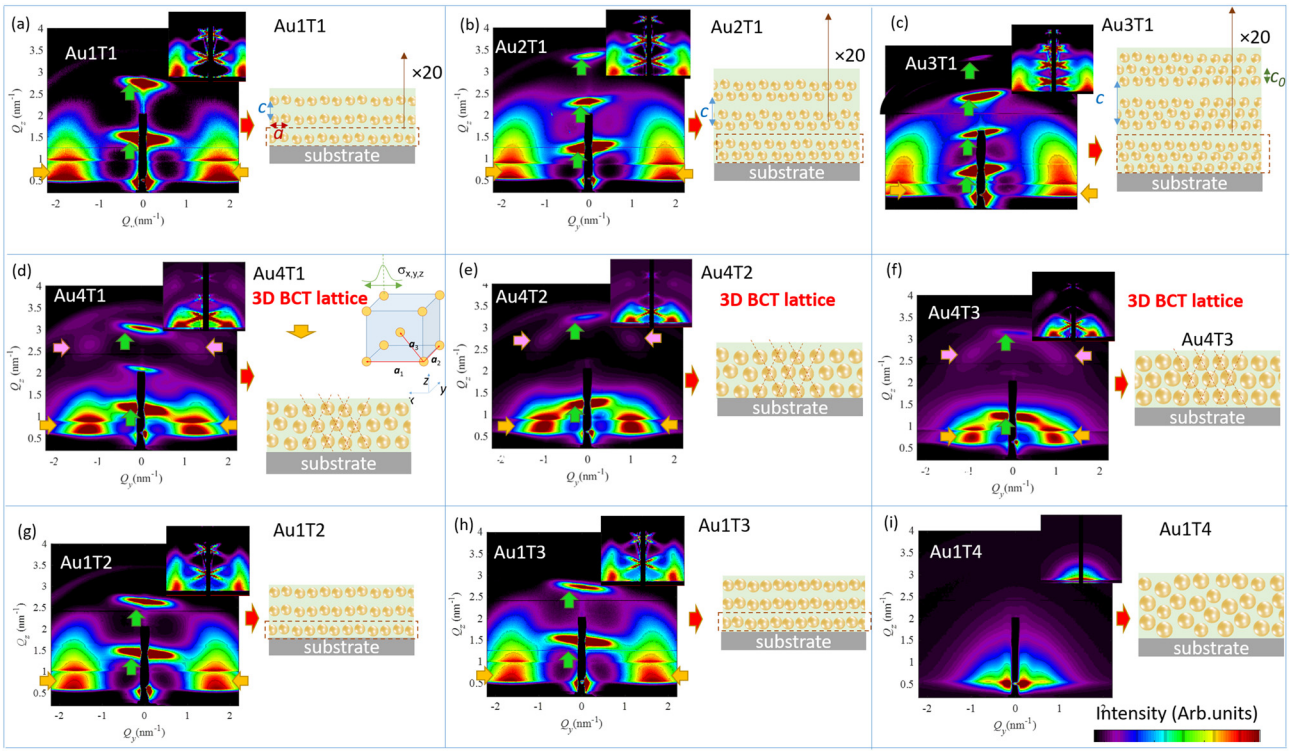

Fig. 1 GISAXS maps, numerical simulations, and schematic representations of Au NP lattices. Distinct intensity peaks confirm ordered NP arrangements; the central dark rectangle corresponds to the beam stop.

Open Access Article. Published on 13 January 2026. Downloaded on 5/1/2026 4:58:18 PM.
This article is licensed under a Creative Commons Attribution 3.0 Unported Licence.

Table 2 Parameters of the Au QD lattices found by GISAXS analysis and their errors. *a* and *c* are the lateral and vertical separation of Au NPs, respectively. $\sigma_{1-3}^{x,y,z}$ are the deviation parameters, σ_R is standard deviation of the size distribution, and R_L and R_V are the Au NP lateral and vertical radii, respectively. *d* is the thickness of the films. All values are given in nm

Sample/par	*a*	*c*	$\sigma_{1,2}^{x,y}$	$\sigma_{1,2}^{z}$	$\sigma_{3}^{x,y}$	σ_{3}^{z}	R_L	R_V	σ_R	*d*
Au1T1	3.2	4.6	1.0	0.2	1.1	0.2	0.84	1.0	0.07	92.0
Au2T1	3.1	2.4	1.1	0.2	1.2	0.2	0.84	0.96	0.08	48.0
Au3T1	2.9	2.0	1.2	0.2	1.3	0.2	0.83	0.08		40.0
Au4T1	4.0	5.9	1.3	0.5	1.3	0.2	1.75	1.75	0.15	118.0
Au4T2	4.5	5.9	1.7	0.1	1.0	0.2	1.9	1.9	0.2	118.0
Au4T3	4.9	5.9	1.9	0.1	1.3	0.2	2.0	2.0	0.2	118.0
Au1T2	3.3	4.6	1.1	0.2	1.6	0.2	0.86	1.01	0.10	92.0
Au1T3	3.5	4.3	0.9	0.4	1.0	0.3	1.0	0.94	0.11	86.0
Au1T4	—	—	—	—	—	—	1.9	1.9	0.22	82.0

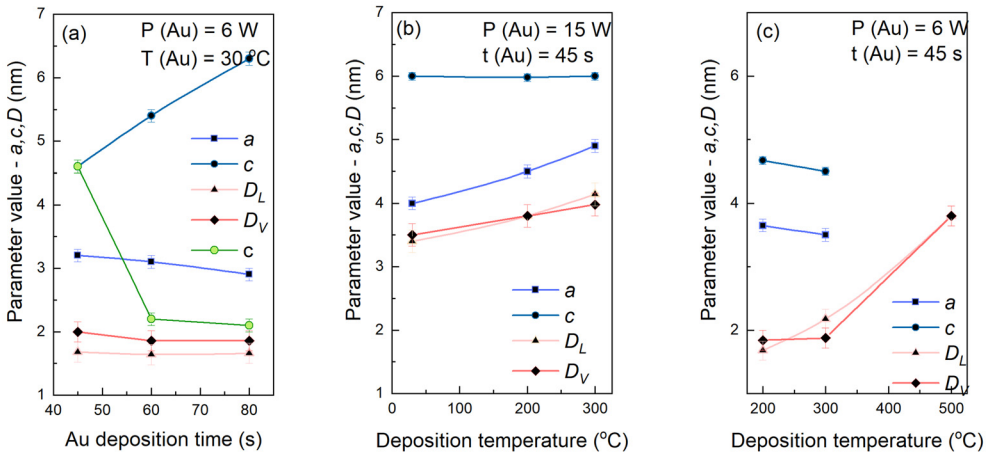

Fig. 2 Dependence of the Au NP separations (*a*-lateral and *c*-vertical), and their diameters (D_L and D_V) on the (a) Au deposition time, and (b)–(c) deposition temperature. In panel (a) parameter *c* labeled by green color corresponds to the multilayer spacing. In panels (b) and (c) the multilayer period is equal to the vertical NP separation since each layer has only one sheet of NPs.

spacing. The NP diameters increase significantly above 300 °C, consistent with thermal coarsening. The determined NP radii, lattice parameters and their standard deviations, shown in Table 2, are used to plot the statistical distributions of the NP radii, and their first neighbor separations. They are shown in Fig. S2, SI, and they are used for calculations of the LSPR positions caused by plasmon coupling.

In total, nine distinct lattice configurations are realized, ranging from quasi-2D multilayered arrays to fully ordered 3D BCT structures. These results demonstrate that the multilayer deposition strategy provides precise structural control over the NP arrangements simply by adjusting the Au loading and substrate temperature.

3.1.2. Nanoparticle internal structure–crystalline properties. The crystalline structure of Au NPs and the MoO_3 matrix is examined by grazing-incidence X-ray diffraction (XRD). Diffractograms (Fig. 3) show distinct Au reflections ((111), (200), (220), (311)) at 38.2°, 43.4°, 64.4°, and 77.9°, confirming crystalline Au formation. No peaks corresponding to MoO_3 are visible, indicating that the oxide matrix remains amorphous across all deposition conditions.

All Au-related peaks are broadened, reflecting the small NP size. Peak widths decrease with increasing deposition temperature (for constant Au sputtering power), and are narrower in high-Au-content samples compared to low-Au-content ones at the same temperature (*e.g.*, Au4T2 *vs.* Au1T2). The individual peak contributions to the entire spectrum for three representative films is shown in Fig. 3d. This trend is consistent with the NP growth and coalescence revealed by GISAXS. The crystallite radii are estimated using the Debye–Scherrer formula (Table 3).[46] Although approximate, the derived values are in close agreement with the GISAXS results, further validating the structural model. Together, these data confirm that crystalline Au NPs are embedded in an amorphous MoO_3 host, with their size and spacing finely tuned by the deposition parameters.

3.2. Optical properties of the films

The optical absorption spectra of the films are shown in Fig. 4. While MoO_3 has a low absorption (4 a), the absorbance increases systematically with the Au content: films deposited at higher Au sputtering power (Au4T1–Au4T3, Fig. 4b) exhibit a

 This journal is © The Royal Society of Chemistry 2026

Open Access Article. Published on 13 January 2026. Downloaded on 5/1/2026 4:58:18 PM.
This article is licensed under a Creative Commons Attribution 3.0 Unported Licence.

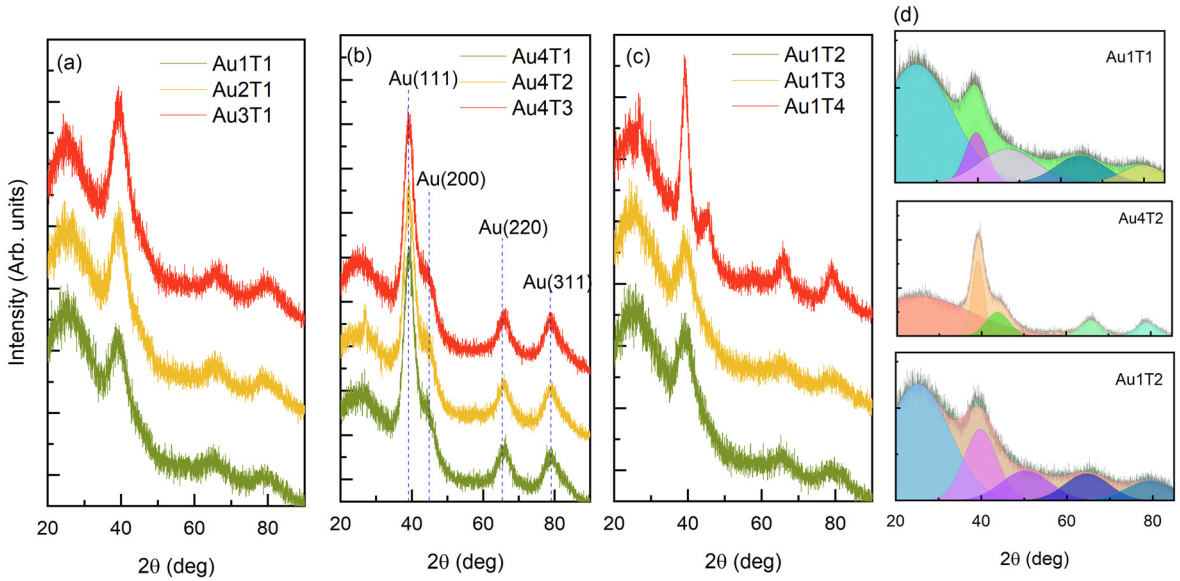

Fig. 3 XRD diffractograms of the Au NPs formed in (a) Au1T1–Au3T1, (b) Au4T1–Au4T3, (c) Au1T2–Au1T4 multilayered (Au + MoO_3)/MoO_3 thin films, and (d) graph showing how the overlapping of individual peaks, due to their large width, hides some parts of the spectrum.

Table 3 Radii of Au NPs in MoO_3 matrix. For each sample, radius is averaged over all visible peaks. FWHM and peak position, together with their standard deviations, are obtained from Gauss fit of the corresponding peak

Sample	Au1T1	Au2T1	Au3T1	Au4T1	Au4T2	Au4T3	Au1T2	Au1T3	Au1T4
R (nm)	1.1 ± 0.1	1.1 ± 0.1	1.1 ± 0.1	2.1 ± 0.2	2.1 ± 0.2	2.1 ± 0.2	1.0 ± 0.1	1.0 ± 0.1	2.0 ± 0.2

markedly higher absorption compared to those with lower Au content (Au1T1–Au3T1, Fig. 4a). Within each series, longer deposition times of the Au–MoO_3 layer also enhance the absorption, as seen in the progression from Au1T1 to Au3T1. These observations are consistent with earlier reports linking the absorption strength to the Au concentration.[31]

All films display clear signatures of localized surface plasmon resonances (LSPR) from Au NPs. The peak position, width, and intensity depend strongly on the deposition conditions. Narrow, well-defined LSPR peaks are observed in Au1T1 and Au1T2, whereas higher-Au-content films (Au4T1–Au4T3) show broad peaks extending to longer wavelengths. The broadening is most pronounced in Au4T3, indicating strong plasmon coupling due to a reduced NP spacing at high Au loading.

To quantify the coupling effect, the lateral and vertical coupling constants are defined as $c_l = d_l/D_L$ and $c_v = d_v/D_V$, where D_L and D_V represent the NP diameters, while d_l and d_v the respective interparticle separations, calculated as $d_l = a - D_l$, and $d_v = c - D_V$. As shown in Fig. 5, large coupling constants (about 1 or greater) are obtained only for Au1T1 and Au1T2, consistent with their narrow LSPR peaks and minimal coupling. In all other films, reduced coupling constants indicate significant plasmon interaction. The peak shifts follow the well-established plasmon "ruler equation":[25,26]

$$\Delta\lambda/\lambda_0 = A\exp^{(-c/\tau)} \quad (1)$$

with τ = 0.23, confirming that the observed red shifts arise from interparticle coupling. The strongest effect is found in Au4T1–Au4T3, where BCT-ordered NP lattices support pronounced plasmon coupling, leading to broad and red-shifted resonance features; the Au4T3 film exhibits the most significant coupling, highlighted in Fig. 5b. These simple coupling parameters provide an intuitive link between lattice geometry and coupling plasmonic response.

Although the BCT geometry in principle supports collective lattice modes (long-range diffractive coupling), in our samples the lattice constants are much smaller than the optical wavelength and the Au NPs are very small (about 2–4 nm).[49] Therefore, near-field LSPR coupling dominates and collective lattice resonances are not expected.

To further predict the LSPR response of non-coupled systems with small NP radii (≈1 nm) we have simulated the absorbed intensity using the modified Mie model described in ref. 50. Unlike the Mie model where size dependence is introduced only *via* the free electron term of Au complex dielectric function, making the damping constant for the free electrons inversely proportional to the NP's radius,[47] the modified Mie model introduces the size dependence by taking into account the intraband transitions. Both models well describe the LSPR

Open Access Article. Published on 13 January 2026. Downloaded on 5/1/2026 4:58:18 PM.
This article is licensed under a Creative Commons Attribution 3.0 Unported Licence.

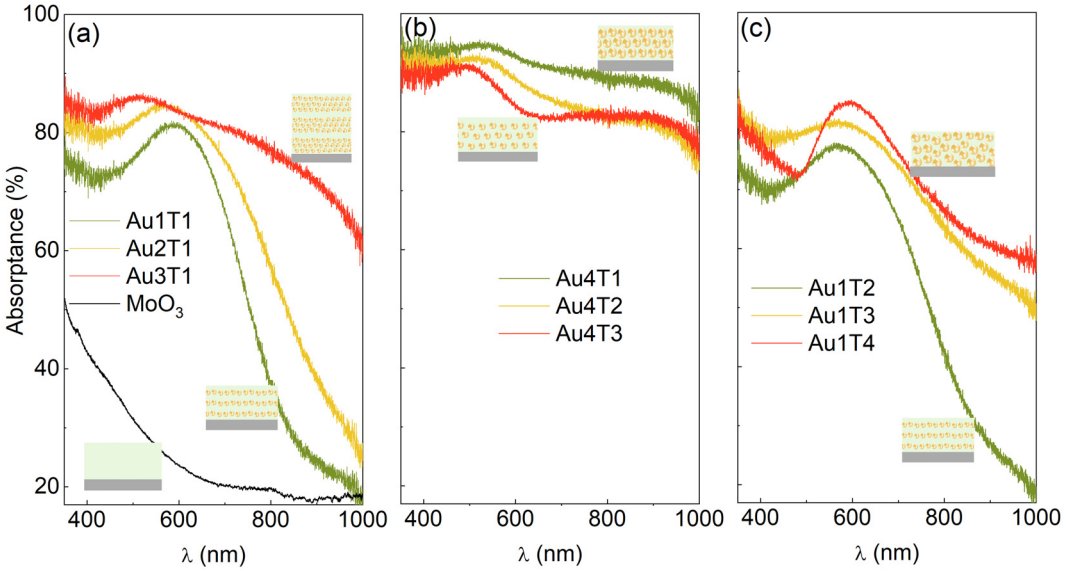

Fig. 4 Optical absorption spectra of Au–MoO_3 films. The presence of gold significantly affects the absorption properties. Films with higher Au content exhibit stronger absorption and broadened LSPR peaks.

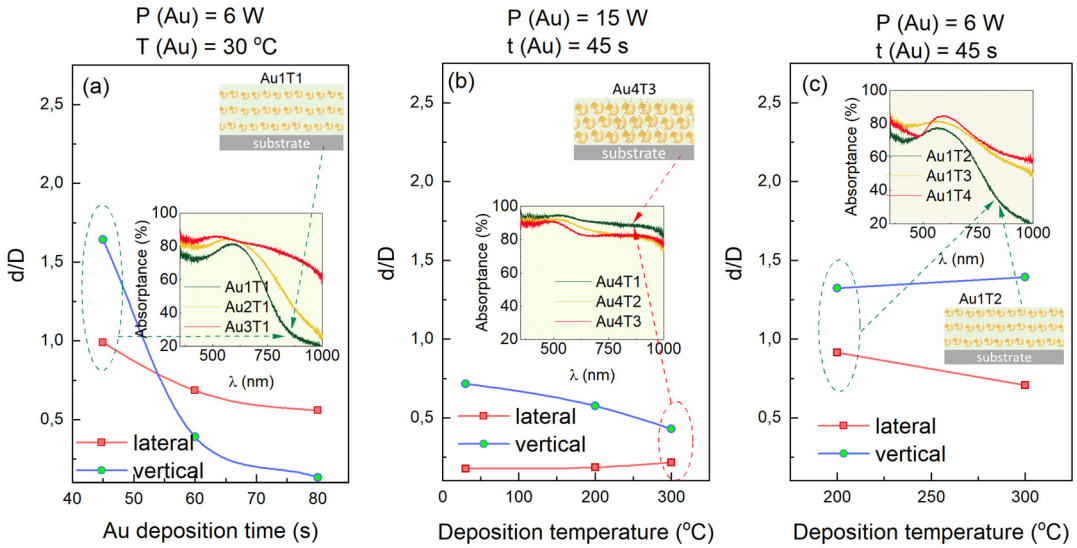

Fig. 5 Coupling constants in lateral (c_l) and vertical (c_v) directions for (a) Au1T1–Au3T1, (b) Au4T1–Au4T3 and (c) Au1T2–Au1T4, NP lattices. Small values (Au4 series) indicate strong plasmon coupling, consistent with broadened and red-shifted LSPR peaks (indicated by dashed red line and arrow), while larger values (>1), denoted by green dashed lines show weak or no coupling resulting in narrow LSPR peaks. Lines are a guide to the eye.

from small Au NPs, like ours. However, the modified one is more suitable for the Au1 NPs with a small number of atoms belonging to the transition regime between non-metallic and metallic behavior (number of atoms per NP is about 170).[51] The result of the simulated absorption at different photon energies as a function of constant C is shown in Fig. 6a, where the position of the SPR peak is clearly indicated. Full details of the modeling procedure are provided in the SI. The experimental data fit best with the modeled intensity for C = 1.5, as indicated by the profile comparison shown in Fig. 6b, where the standard Mie model is also shown. The agreement is good, since the size distribution of Au NPs is not taken into account. In addition, the matrix optical parameters used for the simulation can differ from the real ones due to the high volume content of the gold. For the simulation the optical constants of pure (non-doped) MoO_3 matrix are used. Faceting can significantly influence the plasmonic response,[52] however, the Au NPs studied here are quite small, and no faceting is observed in SEM (Fig. S1). Combined with the GISAXS data indicating spherical symmetry, we conclude that any faceting effects are

 This journal is © The Royal Society of Chemistry 2026

Open Access Article. Published on 13 January 2026. Downloaded on 5/1/2026 4:58:18 PM.
This article is licensed under a Creative Commons Attribution 3.0 Unported Licence.

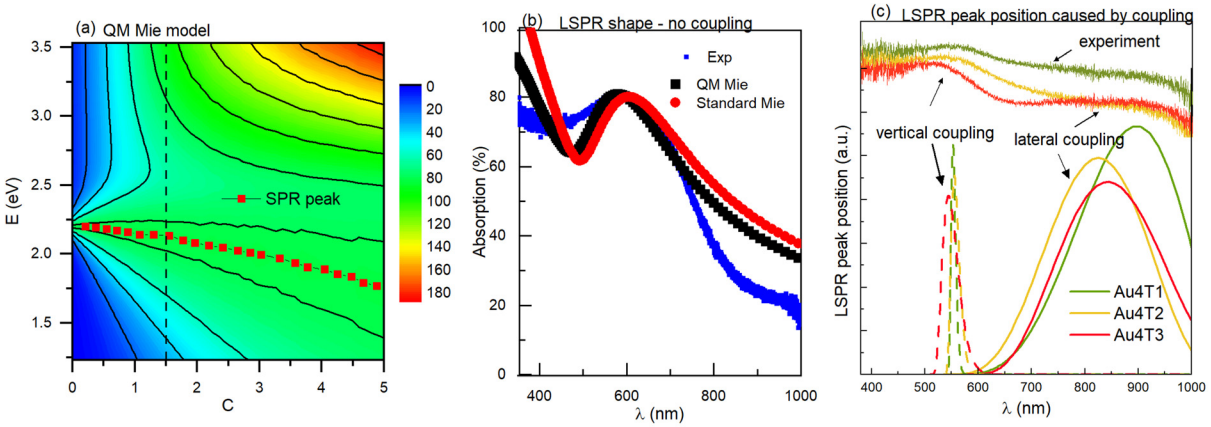

Fig. 6 Simulation of absorbed intensity for different energies and parameter *C*, obtained using Mie model[47] for Au NPs with the radius of 1 nm. The line indicate intensity for $C = 1.5$, which is shown to best agree with the experimental data. (b) Simulated intensity profile along the line $C = 1.5$ using quantum corrected Mie model (black) and standard Mie model with Au dielectric constant taken from Johnson and Christy[48] (red), together with the experimental data (blue). (c) Position of the LSPR peak calculated using the NP separation distributions obtained from GISAXS analysis (see Fig. S2 from SI).

minimal and unlikely to substantially affect the plasmonic properties.

The presented simulations can therefore be used to predict the position and shape of the LSPR for small, non-coupled Au NPs in similar systems, while eqn (1) describes the plasmon coupling effects-that is, the red-shift of the LSPR caused by close interparticle separation. To predict the plasmon peak shift in our system, we used the experimentally determined distributions of Au NP separations from GISAXS analysis (SI Fig. S2(e) and (h)). These distributions were inserted into eqn (1) to calculate the expected LSPR peak positions. As shown in Fig. 6(c), a pronounced red-shift occurs due to strong lateral (in-plane) coupling, whereas the vertical coupling contribution is much smaller. The calculated peak positions are in good agreement with the experimental data presented in Fig. 4.

3.3. Electrical and thermal properties of the films

The electrical resistance of representative Au–MoO_3 multilayer films (Au1T1, Au1T2, Au4T1, Au4T2) and pure MoO_3 is shown in Fig. 7a. All films exhibit semiconducting behavior, with the resistance decreasing as the temperature increases. Pure MoO_3 displays the highest resistance and the strongest temperature dependence, consistent with its insulating nature. While such sensitivity may be useful for temperature-sensing applications, it is generally undesirable for optoelectronic devices requiring a stable operation. The incorporation of Au NPs dramatically reduces the resistance correlated to the amount of Au in the films. The highest decrease is achieved for Au4 films (high Au loading), showing resistances up to six orders of magnitude lower than MoO_3. This reduction is attributed primarily to electrical doping *via* increased carrier density, although factors such as Au–O bonding and enhanced crystallinity may also contribute.[53] Furthermore, higher deposition temperatures consistently decrease the resistance, independent of the Au content.

Using the film thicknesses reported in Table 2 and the measured resistance, the films resistivity at room temperature is calculated. The pure MoO_3 has resistivity of 1.9×10^4 Ωm, what agree well with the literature values. Adding the gold significantly decreases it, so the film Au1T1 has resistivity of 44.5 Ωm, while the film Au4T1 has 3.5×10^{-2} Ωm. This value is about thousand time less than for the film Au1T1 and 5×10^5 times less than the pure MoO_3 film.

Activation energies (E_A) are determined from Arrhenius plots (Fig. 7b). The values span from 160 meV for Au1T2 to only 21 meV for Au4T2, indicating that higher Au incorporation substantially lowers the thermal barrier for carrier transport. The temperature coefficient of resistance (TCR) is also evaluated (Fig. 7c). TCR, defined as

$$\mathrm{TCR} = \mathrm{d}R/R\mathrm{d}T = -E_A/k_B T^2 \quad (2)$$

scales directly with the activation energy. Pure MoO_3 exhibits very high TCR, reflecting its strong thermal sensitivity, whereas Au4 films display values nearly 50 times smaller, approaching zero. Au1 samples show slightly larger TCR with a weak negative slope, consistent with their higher E_A. Overall, the addition of Au NPs strongly suppresses the TCR, improving the thermal stability of MoO_3-based films for device applications.

The dependence of resistance and activation energy on the structural parameters is summarized in Fig. 8. The resistance decreases by close to six orders of magnitude as the Au volume fraction increases to about 0.3 (Fig. 8a), while the opposite trend is observed when the normalized interparticle spacing (d/D ratio) increases (Fig. 8b). The activation energy exhibits the same trend as resistance where it decreases by two orders of magnitude with increasing Au volume fraction (Fig. 8c) and increases with an increasing d/D ratio (Fig. 8d). This behavior indicates that charge transport is dominated by interparticle tunneling across MoO_3

Open Access Article. Published on 13 January 2026. Downloaded on 5/1/2026 4:58:18 PM.
This article is licensed under a Creative Commons Attribution 3.0 Unported Licence.

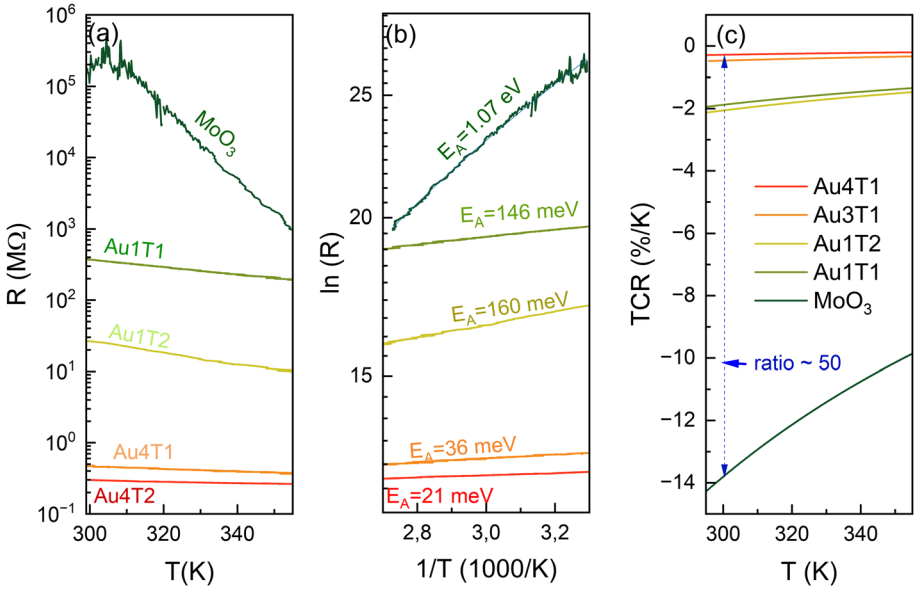

Fig. 7 Electrical transport of Au–MoO_3 films. (a) Resistance *vs.* temperature. (b) Arrhenius plots used to extract activation energies (E_A). (c) Temperature coefficient of resistance (TCR), showing strong suppression upon Au incorporation.

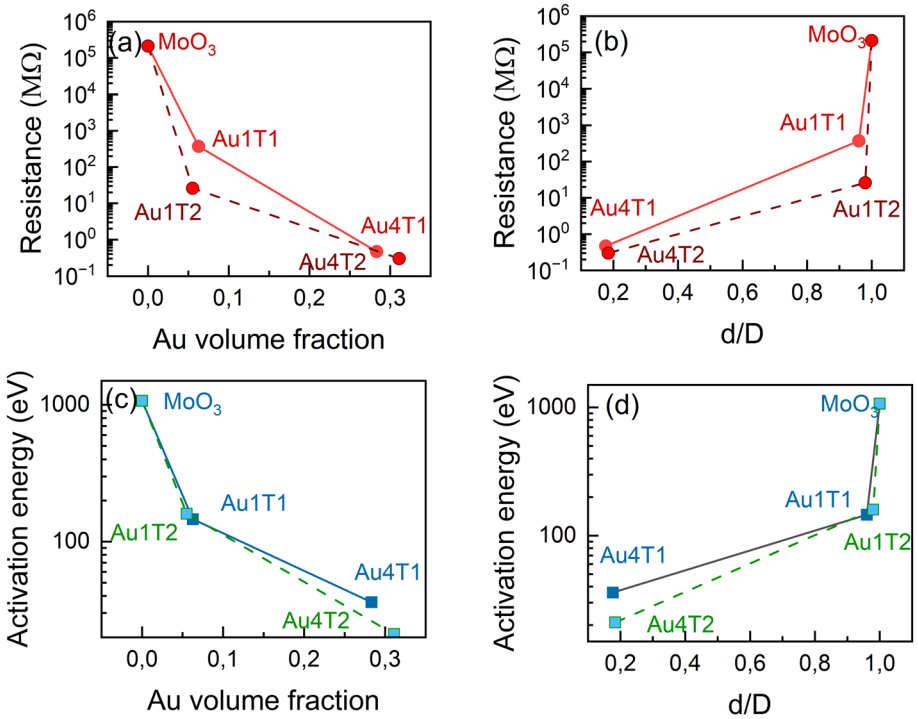

Fig. 8 Dependence of resistance (a, c) and activation energy (b, d) on Au volume fraction and normalized NP spacing (d/D). Resistance reduction with higher Au content and smaller interparticle spacing supports tunneling-dominated conduction.

barriers. In assemblies of metallic NPs, two mechanisms-tunneling and hopping-typically govern carrier transport.[32] Here, the pronounced sensitivity of the resistance to the NP spacing strongly supports tunneling as the dominant conduction pathway (Fig. 8b), in agreement with previous reports.[54]

4. Conclusion

We have demonstrated that magnetron co-sputtering enables the fabrication of multilayer Au–MoO_3 thin films containing well-defined three-dimensional Au nanoparticle lattices. By systematically varying the Au deposition power, deposition

 This journal is © The Royal Society of Chemistry 2026

Open Access Article. Published on 13 January 2026. Downloaded on 5/1/2026 4:58:18 PM. This article is licensed under a Creative Commons Attribution 3.0 Unported Licence.

time, and substrate temperature, we achieved precise control over the nanoparticle size, arrangement, and interparticle spacing. GISAXS measurements confirmed the formation of ordered spherical Au NPs, arranged as periodically spaced sheets in the Au1T1–Au3T1 samples and as body-centered tetragonal (BCT) lattices in the Au4T1–Au4T3 films. The structural analysis further revealed that the MoO_3 matrix remains amorphous, embedding crystalline Au nanoparticles with nanometer dimensions. Optical measurements showed that the incorporation of Au NPs significantly enhances absorption and introduces LSPR features whose intensity, width, and spectral position depend on the NP size and arrangement. Films with high Au loading (Au4 series) exhibited pronounced plasmon coupling, leading to broadened and red-shifted resonances, in good agreement with theoretical predictions. Electrical transport measurements revealed that pure MoO_3 exhibits a very high resistance and strong thermal sensitivity, while the introduction of Au lattices reduces the resistance by several orders of magnitude and suppresses the TCR by up to fifty-fold. The activation energies decreased with increasing Au content and reduced the NP separation, consistent with tunneling-dominated carrier transport through the MoO_3 barriers. Taken together, these findings demonstrate that embedding ordered Au NP lattices into MoO_3 provides a scalable and highly effective strategy to tailor optical absorption and electrical transport simultaneously. By bridging plasmonics with transition-metal oxide semiconductors, this approach opens new avenues for designing multifunctional materials for optoelectronics, sensing, and energy-conversion applications. Overall, this study highlights a scalable thin-film fabrication strategy that integrates structural control at the nanoscale with functional tunability, making ordered Au–MoO_3 nanocomposites a promising materials platform for nanoscale electronics, plasmonic sensing, and energy-conversion technologies.

Author contributions

Conceptualization, S. I. and M. M.; methodology, S. I., S. B., and M. M.; software, M. M.; formal analysis, S. I., M. Đ., I. P., M. M.; data curation, S. I., J. D, M. Đ., I. Š., S. B.; writing – original draft preparation, S. I. writing – review and editing, all authors.; visualization, S. I. and M. M.; project administration, M. M.; funding acquisition, M. M. All authors have read and agreed to the published version of the manuscript.

Conflicts of interest

The authors declare no conflict of interest. The founders had no role in the design of the study; in the collection, analyses, or interpretation of data; in the writing of the manuscript, or in the decision to publish the results.

Data availability

Data for this article, including GISAXS, XRD, optical and thermo-electrical measurements are available to download from https://doi.org/10.17632/pnd3bfw4fw.1, Maja Mičetić, Senad Isaković, Juraj Držić, Ivana Periša, Tihomir Car, Sigrid Bernstorff, Maja Đekić (2025), "3D Au Nanoparticle Lattices in MoO_3 for Tunable Optical and Thermo-Electrical Properties", Mendeley Data, V1, DOI: 10.17632/pnd3bfw4fw.1.

Supplemetary materials provide Scanning electron microscopy analysis of the materials, statistical distribution of the Au nanoparticle sizes and seperations, and theoretical model describing optical extinction spectra. See DOI: https://doi.org/10.1039/d5nr03899e.

Acknowledgements

The authors acknowledge Joško Erceg for the preparation of thin films, and Marijan Marciuš for SEM measurements. The research is funded by Croatian Science Foundation pr. No. IP-2022-10-3765.

References

1 H. Kong, E. Ahn, S. Ryu, J. W. Kim, J. Cho, S. Park, D. Kim, G.-S. Jeen and I. Lee, *J. Mater. Sci.*, 2016, **51**, 8928–8934.
2 Ü. Akın and H. Šafak, *J. Alloys Compd.*, 2015, **647**, 146–151.
3 K. Koike, R. Wada, S. Yagi, Y. Harada, S. Sasa and M. Yano, *Jpn. J. Appl. Phys.*, 2014, **53**, 05FJ02.
4 C. Julien, L. El-Farh, M. Balkanski, O. M. Hussain and G. A. Nazri, *Appl. Surf. Sci.*, 1993, **65–66**, 325–330.
5 J. Scarmínio, A. Lourenco and A. Gorenstein, *Thin Solid Films*, 1997, **302**, 66–70.
6 M. Quevedo-lopez, R. Ramírez-Bon, R. A. Orozco-Terán, O. Mendoza-González and O. Zelaya-Angel, *Thin Solid Films*, 1999, **343–344**, 202–205.
7 J. Haber and L. Erwin, *Catal. Today*, 1997, **33**, 119–137.
8 *Handbook of Nanocomposite Supercapacitor Materials I*, ed. K. K. Kar, Springer Nature Switzerland AG, Gewerbestrasse 11, 6330 Cham, Switzerland, 2020.
9 C. Imawan, H. Steffes, F. Solzbacher and E. Obermeier, *Sens. Actuators, B*, 2001, **70**, 119–125.
10 N. Chaturvedi, S. K. Swami and V. Dutta, *Sol. Energy*, 2016, **137**, 379–384.
11 S. Fatima, Y. Gu, S. J. Yang, S. Kutagulla, S. Rizwan and D. Akinwande, *ACS Appl. Mater. Interfaces*, 2023, **15**, 16308–16316.
12 X. Hou, M. Ruan, L. Zhou, J. Wu, B. Meng, W. Huang, K. Zhong, K. Yang, Z. Fang and K. Xie, *J. Energy Chem.*, 2023, **78**, 91–101.
13 Y. Jia and Y. Ma, *J. Energy Storage*, 2024, **85**, 111103.
14 Y. He, H. Tang, Y. Huang, K. Chen, G. Wang, D. Zheng, W. Xu, F. Wang and X. Lu, *Electrochim. Acta*, 2023, **465**, 142988.

Open Access Article. Published on 13 January 2026. Downloaded on 5/1/2026 4:58:18 PM. This article is licensed under a Creative Commons Attribution 3.0 Unported Licence.

15 V. Nirupana and S. Uthnna, *J. Mater. Sci.: Mater. Electron.*, 2016, **27**, 3668–34674.
16 A. T. Güntner, M. Righettoni and S. E. Pratsinis, *Sens. Actuators, B*, 2016, **223**, 266–273.
17 Q. Wang, C. Zhou, X. Yan, J. Wang, D. Wang, X. Yuan and X. Cheng, *Energy Technol.*, 2018, **6**, 2367–2373.
18 J. Li, Y. Cheng, J. Zhang, J. Fu, W. Yan and Q. Xu, *ACS Appl. Mater. Interfaces*, 2019, **11**, 27798–27804.
19 F. H. Alkallas, A. B. G. Trabelsi, M. Shkir and S. A. AlFaify, *Nanomaterials*, 2022, **12**, 2797.
20 R. O. Ijeh, A. C. Nwanya, A. C. Nkele, I. G. Madiba, A. K. H. Bashir, A. B. C. Ekwealor, R. U. Osuji, M. Maaza and F. Ezema, *Ceram. Int.*, 2020, **46**, 10820–10828.
21 V. Amendola, R. Pilot, M. Frasconi, O. M. Maragò and M. A. Iatì, *J. Phys.: Condens. Matter*, 2017, **29**, 203002.
22 A. J. Haes, C. L. Haynes, A. D. McFarland, G. C. Schatz, R. P. V. Duyne and S. Zou, *MRS Bull.*, 2005, **30**, 368–375.
23 Y. Xia and N. J. Halas, *MRS Bull.*, 2005, **30**, 338–348.
24 J. Borges, M. Buljan, J. Sancho-Parramon, I. Bogdanovic-Radovic, Z. Siketic, T. Scherer, C. Kübel, S. Bernstorff, A. Cavaleiro, F. Vaz and A. G. Rolo, *J. Nanopart. Res.*, 2014, **16**, 2790.
25 P. K. Jain, W. Huang and M. A. El-Sayed, *Nano Lett.*, 2007, **7**, 2080–2088.
26 X. Ben and H. S. Park, *J. Phys. Chem. C*, 2011, **115**, 15915–15926.
27 T. He, Y. Ma, Y. Cao, P. Jiang, X. Zhang, W. Yang and J. Yao, *Langmuir*, 2001, **17**, 8024–8027.
28 N. Kumar, H. B. Lee, S. Hwang, T.-W. Kim and J.-W. Kang, *J. Alloys Compd.*, 2019, **775**, 39–50.
29 D. K. Choi, D. H. Kim, C. M. Lee, H. Hafeez, S. Sarker, J. S. Yang, H. J. Chae, G.-W. Jeong, D. H. Choi, T. W. Kim, S. Yoo, J. Song, B. S. Ma, T.-S. Kim, C. H. Kim, H. J. Lee, J. W. Lee, D. Kim, T.-S. Bae, S. M. Yu, Y.-C. Kang, J. Park, K.-H. Kim, M. Sujak, M. Song, C.-S. Kim and S. Y. Ryu, *Nat. Commun.*, 2021, **12**, 2864.
30 H. M. M. Munasinghe Arachchige, D. Zappa, N. Poli, N. Gunawardhana and E. Comini, *Sens. Actuators, B*, 2018, **269**, 331–339.
31 S. Isaković, M. Đekić, M. Tkalčević, D. Boršćak,]sr] I. Periša, S. Bernstorff and M. Mičetić, *Crystals*, 2022, **12**, 1361.
32 T. Car, A. Šantić, N. Ray, N. Nekić, K. Salamon, S. Bernstorff and M. Buljan, *Appl. Phys. Lett.*, 2017, **111**, 172104.
33 M. Buljan, U. V. Desnica, M. Ivanda, N. Radić, P. Dubček, G. Dražić, K. Salamon, S. Bernstorff and V. Holý, *Phys. Rev. B: Condens. Matter Mater. Phys.*, 2009, **79**, 035310.
34 T. Car, I. Jakovac, I. Šarić, S. Bernstorff and M. Mičetić, *Materials*, 2021, **14**, 766.
35 L. Basioli, M. Tkalčević, I. Bogdanović-Radović, G. Dražić, P. Nadazdy, P. Siffalovic, K. Salamon and M. Mičetić, *Nanomaterials*, 2020, **10**, 1363.
36 N. Nekić, I. Šarić, K. Salamon, L. Basioli, J. Sancho-Parramon, J. Grenzer, R. Hübner, S. Bernstorff, M. Petravić and M. Mičetić, *Nanotechnology*, 2019, **30**, 335601.
37 J. Okumu, C. Dahmen, A. N. Sprafke, M. Luysberg, G. von Plessen and M. Wuttig, *J. Appl. Phys.*, 2005, **97**, 094305.
38 Y. Hatakeyama, K. Onishi and K. Nishikawa, *RSC Adv.*, 2011, **1**, 1815–1821.
39 M. Buljan, N. Radić, S. Bernstorff, G. Dražić, I. Bogdanović-Radović and V. Holý, *Acta Crystallogr., Sect. A: Found. Crystallogr.*, 2012, **68**, 124–138.
40 L. Basioli, K. Salamon, M. Tkalčević, I. Mekterović, S. Bernstorff and M. Mičetić, *Crystals*, 2019, **9**, 479.
41 M. Buljan, N. Radić, M. Ivanda, I. Bogdanović-Radović, M. Karlušić, J. Grenzer, S. Prucnal, G. Dražić, G. Pletikapić, V. Svetličić, M. Jerčinović, S. Bernstorff and V. Holý, *J. Nanopart. Res.*, 2013, **15**, 1485.
42 M. Buljan, N. Radić, J. Sancho-Paramon, V. Janicki, J. Grenzer, I. Bogdanović-Radović, Z. Siketić, M. Ivanda, A. Utrobičić, R. Hübner, R. Weidauer, V. Valeš, J. Endres, T. Car, M. Jerčinović, J. Roško, S. Bernstorff and V. Holy, *Nanotechnology*, 2015, **26**, 065602.
43 N. Nekić, J. Sancho-Parramon, I. Bogdanović-Radović, J. Grenzer, R. Hübner, S. Bernstorff, M. Ivanda and M. Buljan, *Nanophotonics*, 2017, **6**, 1055–1062.
44 I. Hammami, N. M. Alabdallah, A. A. Jomaa and M. Kamoun, *J. King Saud Univ., Sci.*, 2021, **33**, 101560.
45 B. Li, L. Huang, M. Zhou, X. Fan and M. Ma, *J. Wuhan Univ. Technol., Mater. Sci. Ed.*, 2014, **29**, 651–655.
46 J. I. Langford and A. J. C. Wilson, *J. Appl. Crystallogr.*, 1978, **11**, 102–113.
47 M. M. A. Marcos, J. T. Khoury, T. G. Schaaff, M. N. Shafigullin, I. Vezmar and R. L. Whetten, *J. Phys. Chem. B*, 1997, **101**, 3706–3712.
48 P. B. Johnson and R. W. Christy, *Phys. Rev. B*, 1972, **6**, 4370.
49 V. G. Kravets, A. V. Kabashin, W. L. Barnes and A. N. Grigorenko, *Chem. Rev.*, 2018, **118**, 5912–5951.
50 L. B. Scaffardi and J. O. Tocho, *Nanotechnology*, 2006, **17**, 1309–1315.
51 D. Cheng, R. Liu and K. Hu, *Front. Chem.*, 2022, **10 – 2022**, 958626.
52 V. Devaraj, J.-M. Lee, S. Adhikari, M. Kim, D. Lee and J.-W. Oh, *Nanoscale*, 2020, **12**, 22452–22461.
53 D. Cheyns, B. Kam, K. Vasseur, P. Heremans and B. P. Rand, *J. Appl. Phys.*, 2013, **113**, 043109.
54 A. Tackeuchi, T. Kuroda, K. Mase, Y. Nakata and N. Yokoyama, *Phys. Rev. B: Condens. Matter Mater. Phys.*, 2000, **62**, 1568.

This journal is © The Royal Society of Chemistry 2026